SUPPLEMENTAL MATERIALS

Global assessment of the skills of satellite precipitation products to retrieve extreme rainfall events causing landsliding.

Odin MARC,[a] Romulo A JUCÁ OLIVEIRA,[a,b] Marielle GOSSET,[a] Robert EMBERSON,[c, d, e] Jean-Philippe MALET[f]

[a] *Géosciences Environnement Toulouse (GET), UMR 5563, CNRS/IRD/CNES/UPS, Observatoire Midi-Pyrénées, Toulouse, France*

[b] *Laboratoire d'Etudes en Géophysique et Océanographie Spatiales (LEGOS), Université de Toulouse III/CNRS/CNES/IRD, Observatoire Midi-Pyrénées, Toulouse, France*

[c] *NASA Goddard Space Flight Center, Hydrological Sciences Laboratory, United States of America*

[d] *Universities Space Research Association, Columbia, MD, USA*

[e] *NASA Goddard Earth Sciences Technology and Research, Columbia, MD, USA*

[f] *Institut Terre et Environnement de Strasbourg, ITES - CNRS/UMR7063, EOST/Université de Strasbourg, 5 rue Descartes, F-67084 Strasbourg, France.*

Corresponding author: Odin Marc, odin.marc@get.omp.eu

Supplementary methods

Landslide mapping

We have produced new landslides map associated with intense rainfall in Japan 2004 (Kondo et al 2005), Myanmar 2015 (Mondini, 2017) and Haiti 2016. In each cases, comparing pre and post event imagery allowed to visually detect NDVI or reflectances changes associated with the removal of vegetation on hillslopes (Marc et al., 2018).

For Myanmar 2015, we used the catalogue derived from a small area (Mondini, 2017) as a training sample for an automated landslide algorithm (Stumpf et al., 2014) and applied it to two Sentinel-2 images, yielding a more complete inventory over a broader area for this landslide event. Though, we limited our classification to two Sentinel-2 images, some landslides likely from the same event are visible in Google Earth until about 22.4°N 93.7°N, ~25km south of the image boundary (~22.75°N).

In Haiti, many landslides occurred during Hurricane Matthew (Haïti) in early October 2016 in the western tip of Tiburon Peninsula. Using a pair of high resolution images (Spot 6 and 7, 2.5m resolution in panchromatic, 5m in RGB bands) we manually mapped >500 landslides and extended the mapping over the full image with the same semi-automatic landslide mapping algorithm. Again this zone appears to be the most intensely affected though some diffuse landsliding may have occurred in the less steep hills to the east (-74E to -73E), not captured by the images used for mapping.

Last, we also manually mapped the landslides (~80) caused by the Meari typhoon near Miyagawa village in the northeastern part of the Kii peninsula (Japan). In these case we identified vegetation disturbance on hillslopes on a pair of cloud free Landsat 5 images acquired on 15/04/2004 and 04/05/2005, respectively. Then we delineated accurate polygons corresponding to these disturbances, based on high resolution imagery available in Google Earth dated from 2009 (for all landslides north of 34.289°) and from 2012 southward. Many more landslides were visible in the high resolution imagery but could have been caused before or after the event in autumn 2004 and were thus ignored. Indeed, this inventory clearly misses a substantial number of small size landslides (Kondo et al 2005, Shuin et al., 2012), and assumes the landslides' geometries did not change between 2004 and 2009/2012. For the purpose of this study (e.g., delineating the area affected by widespread landsliding) these limitations are not crucial.

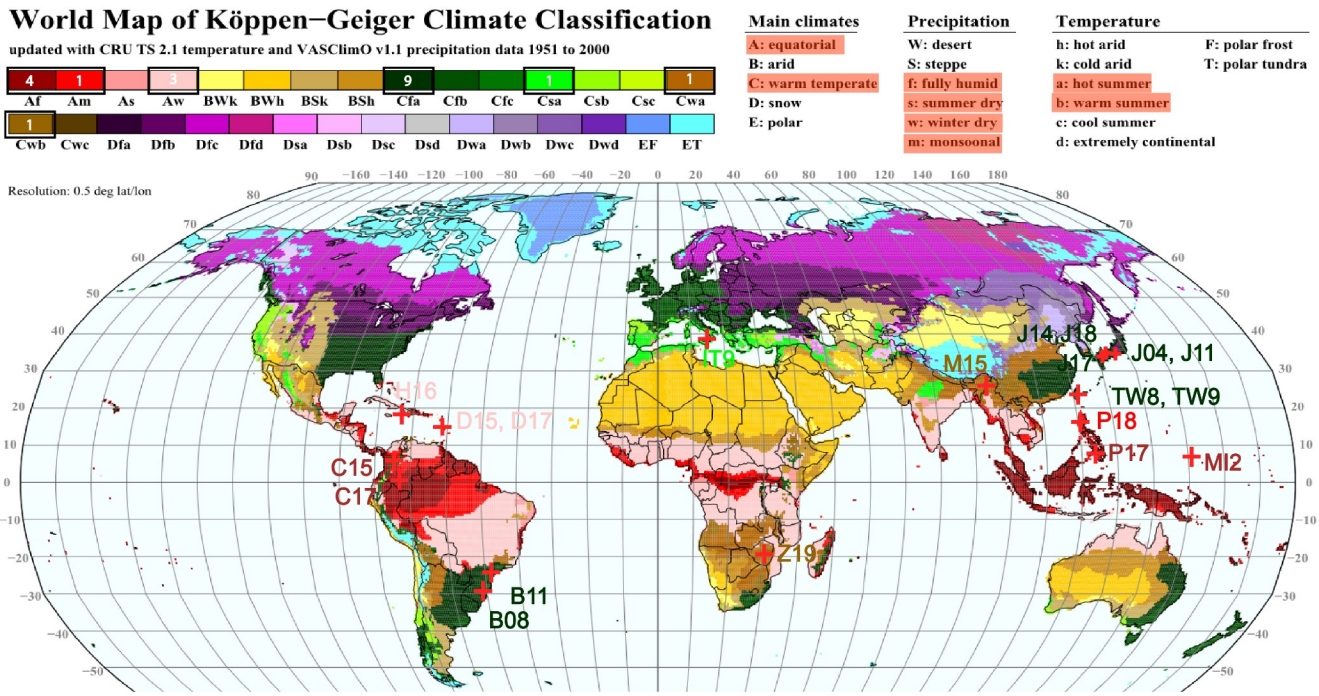

Figure S1: World map of Koppen-Geiger Climate Classification with the locations of the 20 studied widespread landslide events. The name code of each event is color-coded by its local climate. Climate types sampled by the events (mainly warm temperate and equatorial) are highlighted in red and with black box and the associated number of landslide events in the upper left colorbar. Map modified after Kottek et al., 2006.

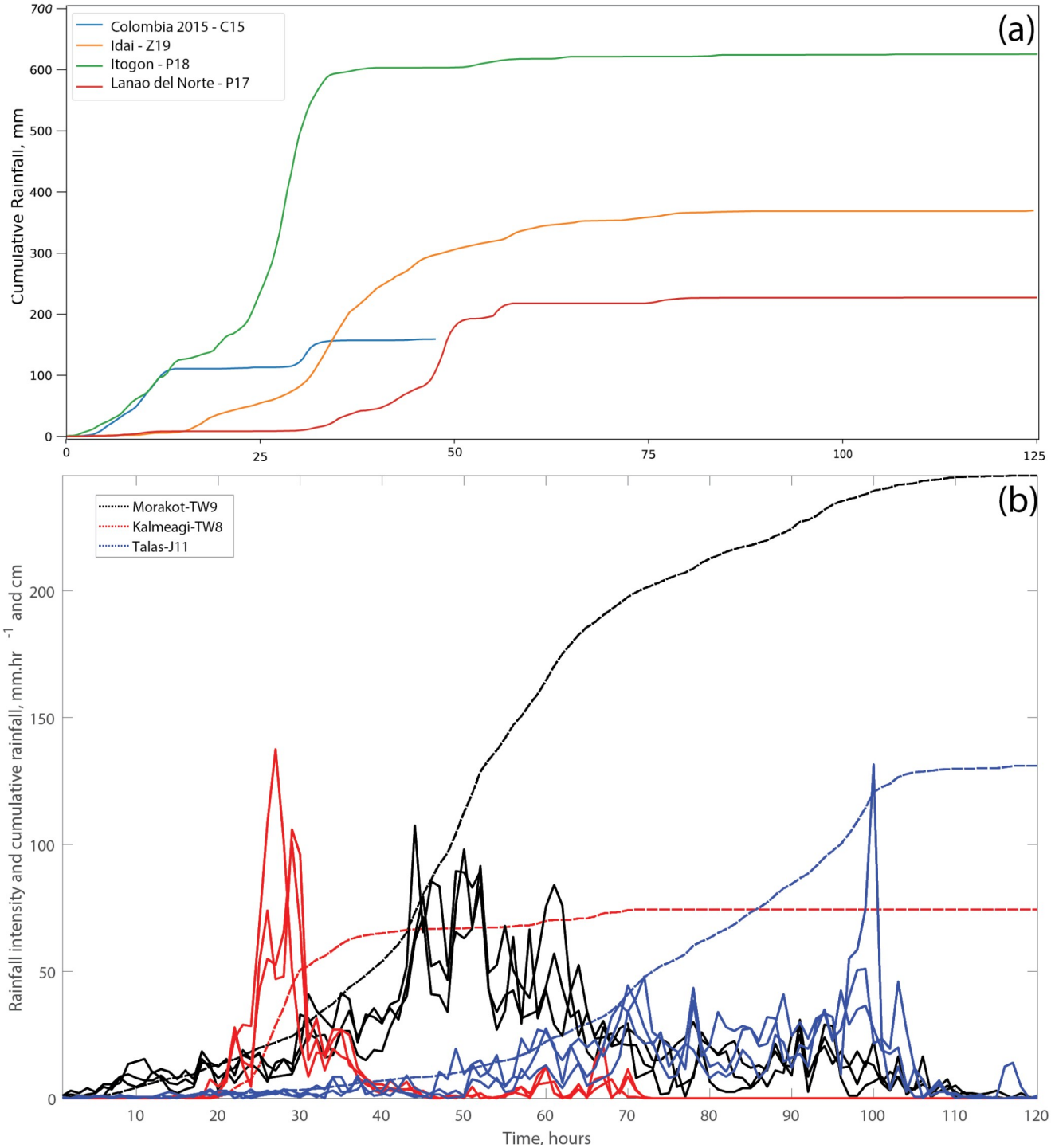

Figure S2: Example of rainfall timeseries for 7 storm events. In (a) we show the cumulative rainfall for 125 hours after the start of rainfall for four events for which in-situ record are not available. The rainfall shown here is derived from the IMERG data for a pixel with the maximum cumulative rainfall within the landslide event area. In (b) we show the rainfall intensity and cumulative rainfall for three gauges near the landslide event areas, as shown by Marc et al., 2018. It is clear from these events that the high intensity rainfall can be sustained for short duration (<10h as in C15), intermediate duration (10-30h as in P17, P18 and TW8) or long duration (30-90h as in Z19, TW9 and J11).

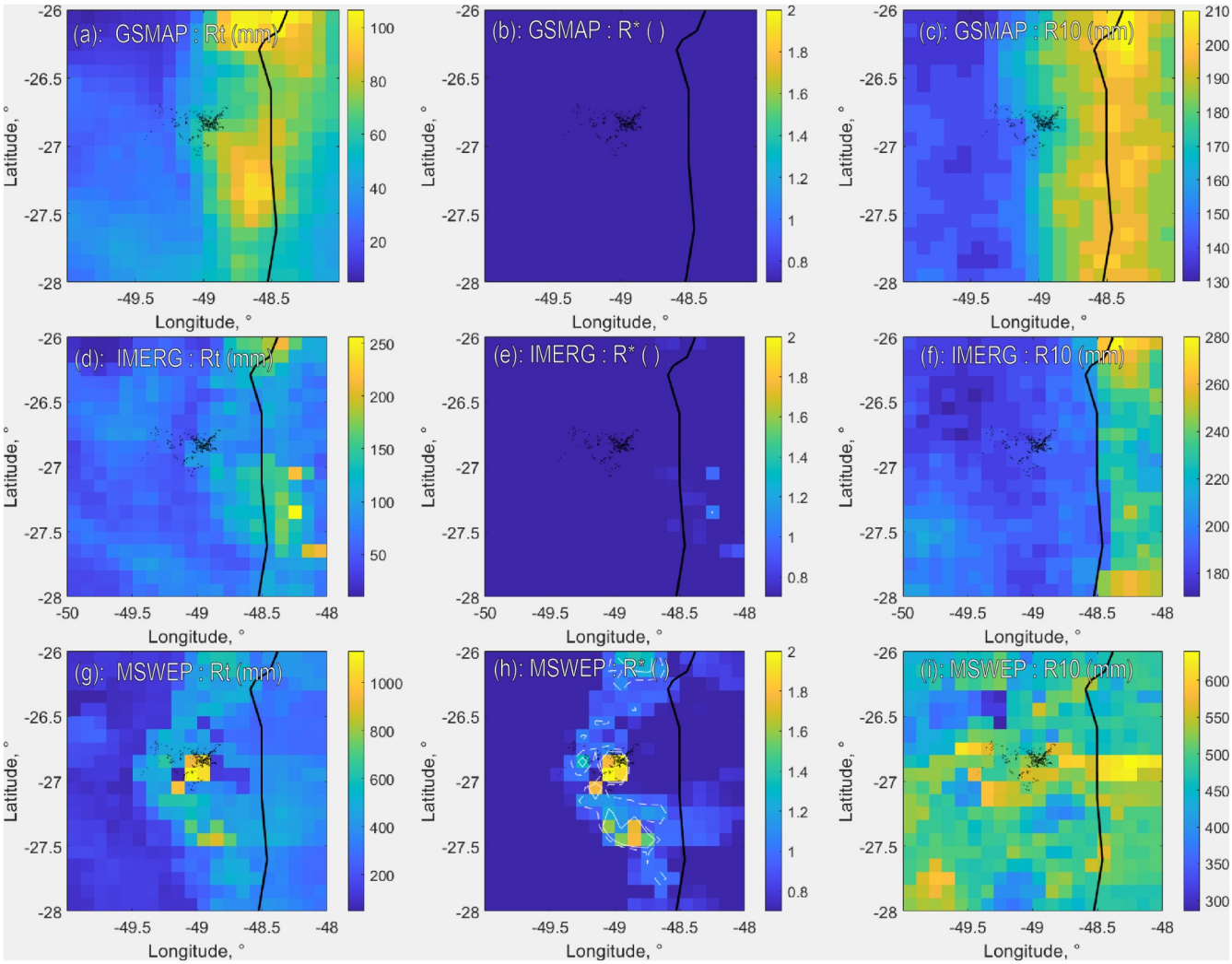

Figure S3 : Maps of the maximum total rainfall, Rt, (a,d,g), the rainfall anomaly, R*, (b,e,h) and the 10 year return rainfall, R10, (c,f,i) at the 48 h time scales for the B08 event derived from GSMAP, IMERG and MSWEP, respectively. Note the different scales for Rt and R10.

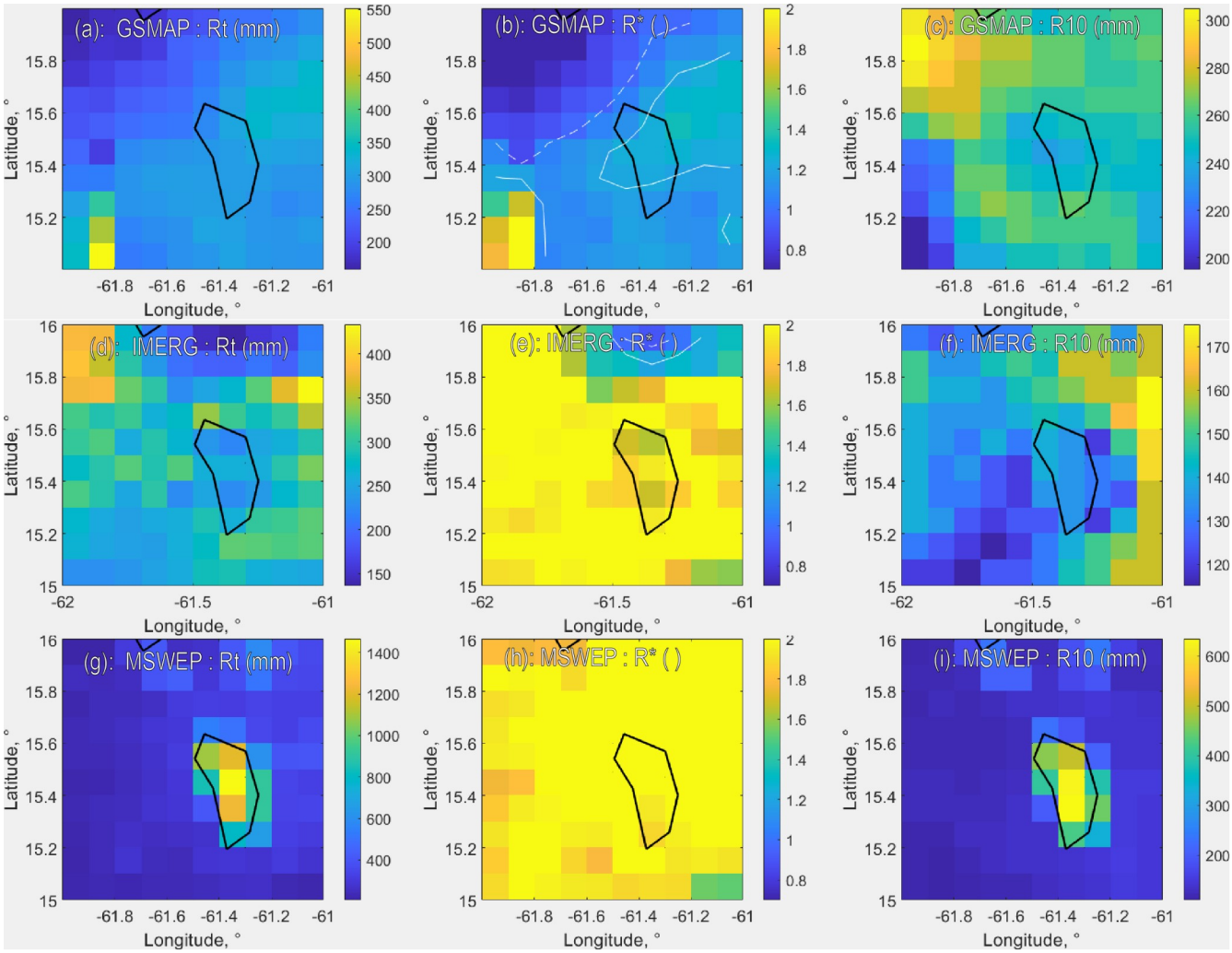

Figure S4 : Maps of the maximum total rainfall, Rt, (a,d,g), the rainfall anomaly, R*, (b,e,h) and the 10 year return rainfall, R10, (c,f,i) at the 12 h time scales for the D15 event derived from GSMAP, IMERG and MSWEP, respectively. Note the different scales for Rt and R10.

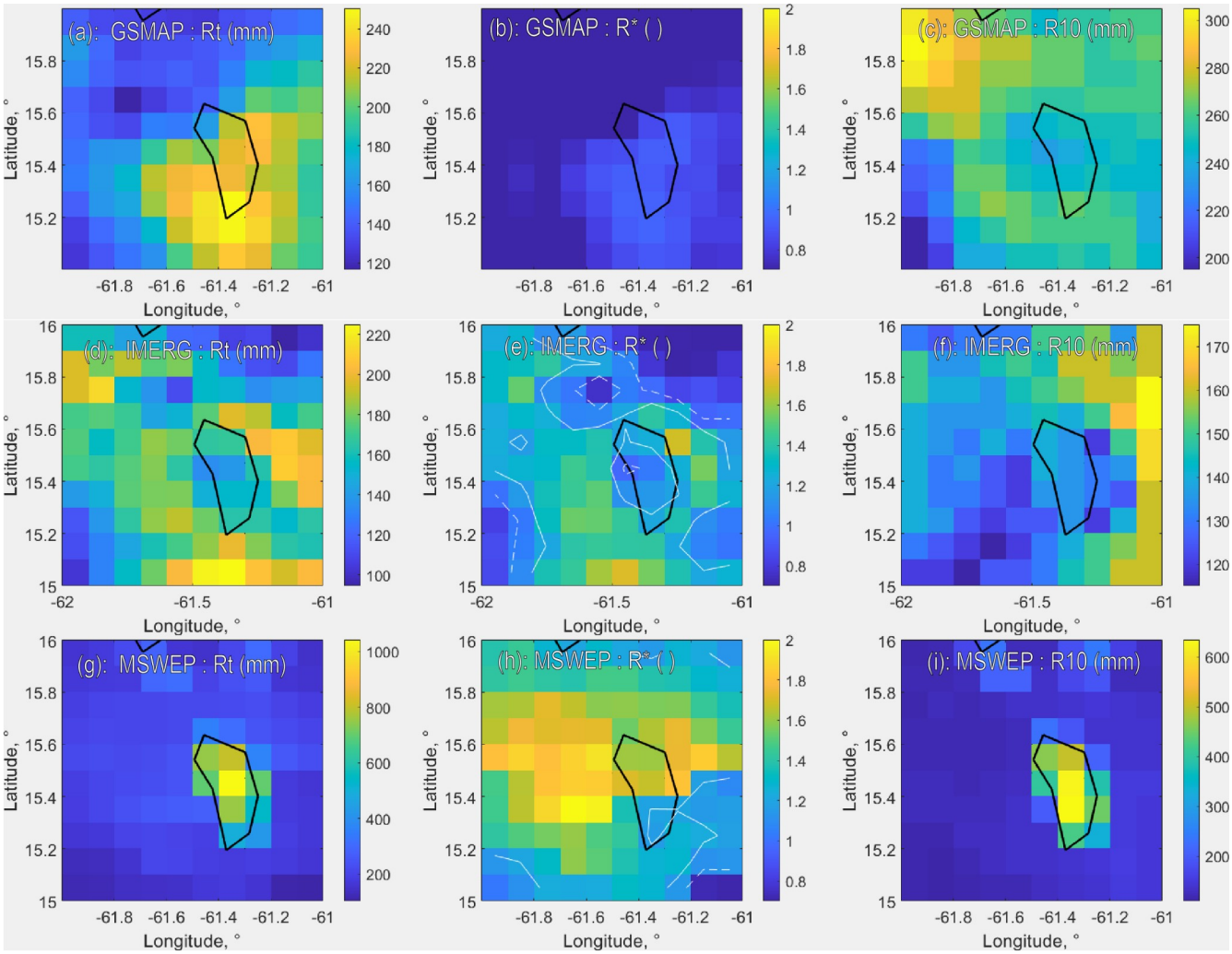

Figure S5 : Maps of the maximum total rainfall, Rt, (a,d,g), the rainfall anomaly, R*, (b,e,h) and the 10 year return rainfall, R10, (c,f,i) at the 12 h time scales for the D17 event derived from GSMAP, IMERG and MSWEP, respectively. Note the different scales for Rt and R10.

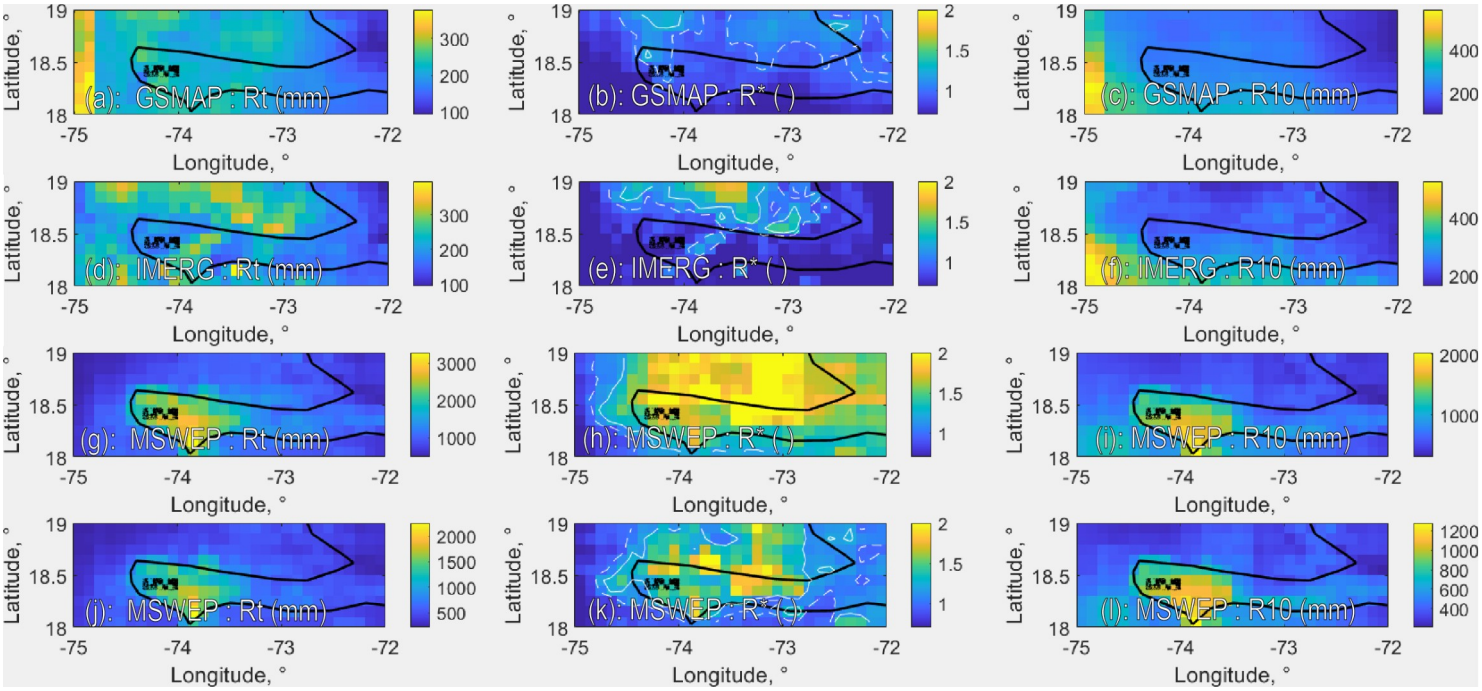

Figure S6 : Maps of the maximum total rainfall, Rt, (a,d,g), the rainfall anomaly, R*, (b,e,h) and the 10 year return rainfall, R10, (c,f,i) at the 48 h time scales for the HAI event derived from GSMAP, IMERG and MSWEP, respectively. Note the different scales for Rt and R10. In (jkl) we show the same for MSWEP at 12h where less overprediction occurs.

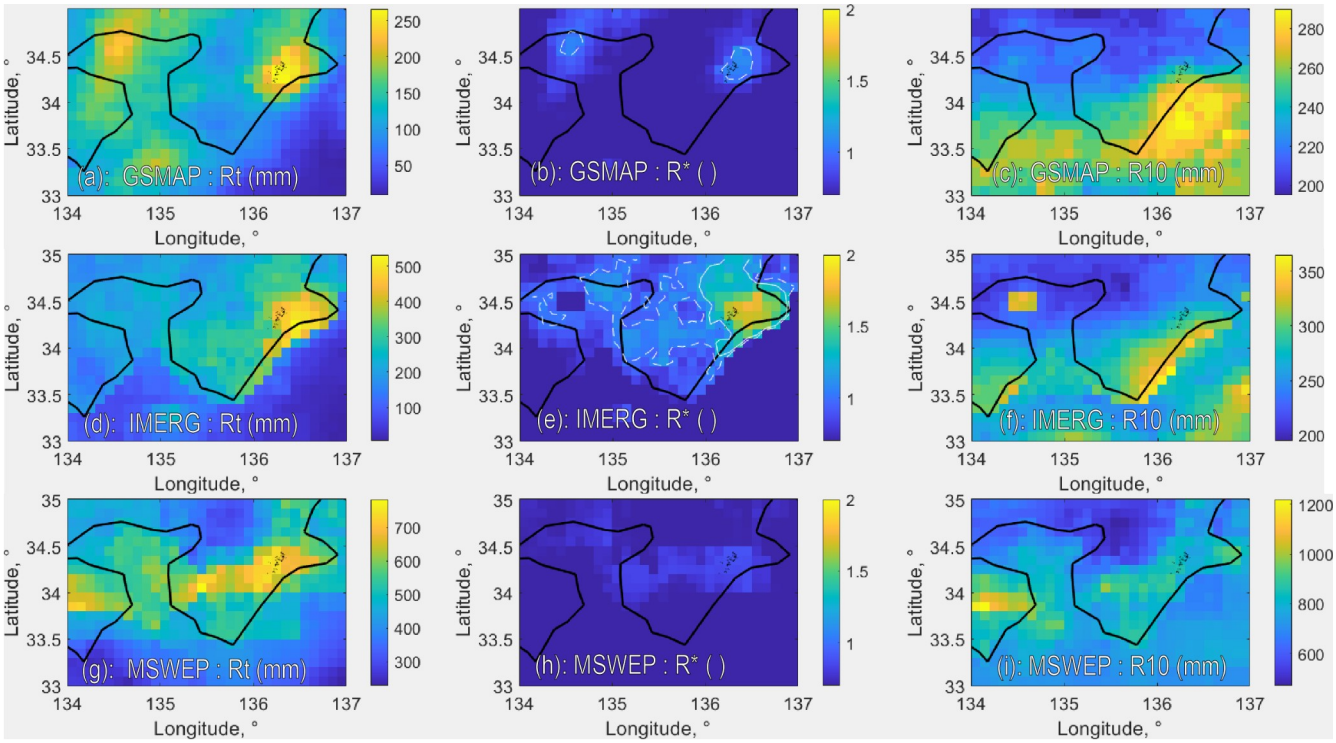

Figure S7 : Maps of the maximum total rainfall, Rt, (a,d,g), the rainfall anomaly, R*, (b,e,h) and the 10 year return rainfall, R10, (c,f,i) at the 48 h time scales for the J04 event derived from GSMAP, IMERG and MSWEP, respectively. Note the different scales for Rt and R10.

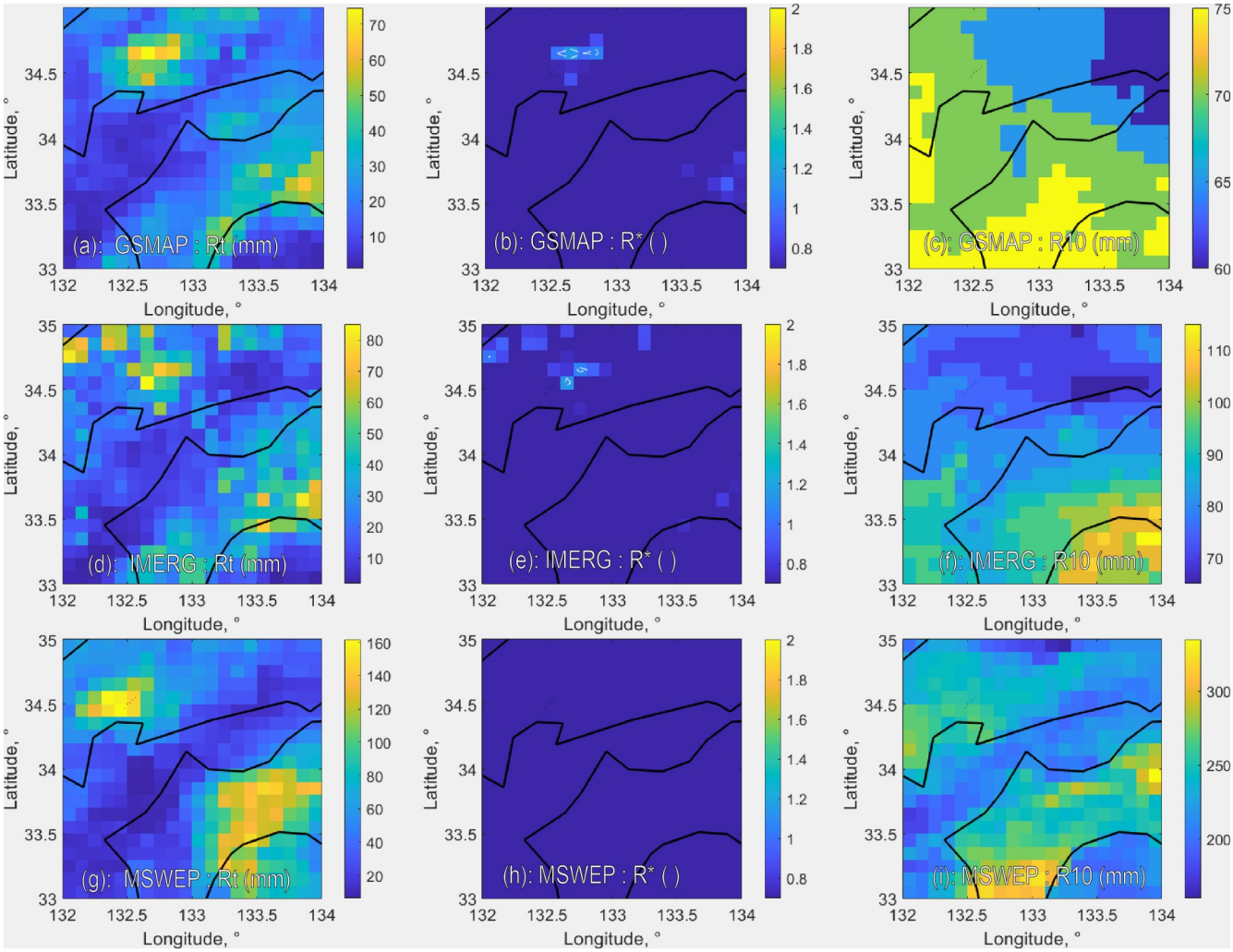

Figure S8 : Maps of the maximum total rainfall, Rt, (a,d,g), the rainfall anomaly, R*, (b,e,h) and the 10 year return rainfall, R10, (c,f,i) at the 3 h time scales for the J14 event derived from GSMAP, IMERG and MSWEP, respectively. Note the different scales for Rt and R10.

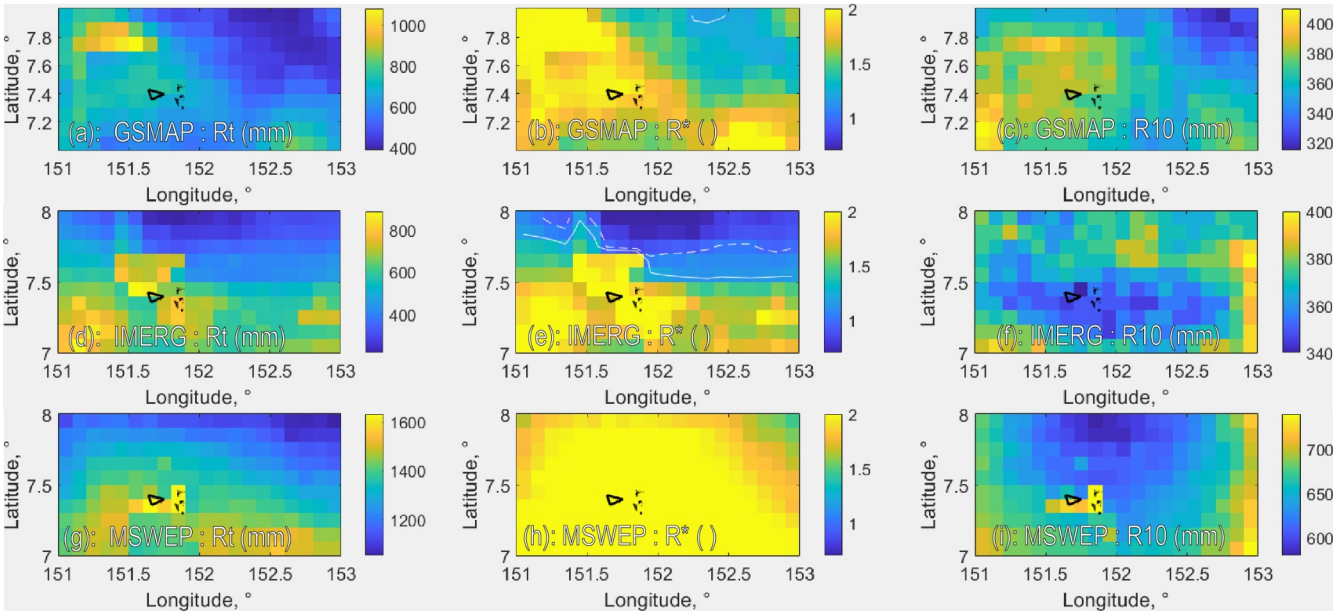

Figure S9 : Maps of the maximum total rainfall, Rt, (a,d,g), the rainfall anomaly, R*, (b,e,h) and the 10 year return rainfall, R10, (c,f,i) at the 48 h time scales for the MIC event derived from GSMAP, IMERG and MSWEP, respectively. Note the different scales for Rt and R10.

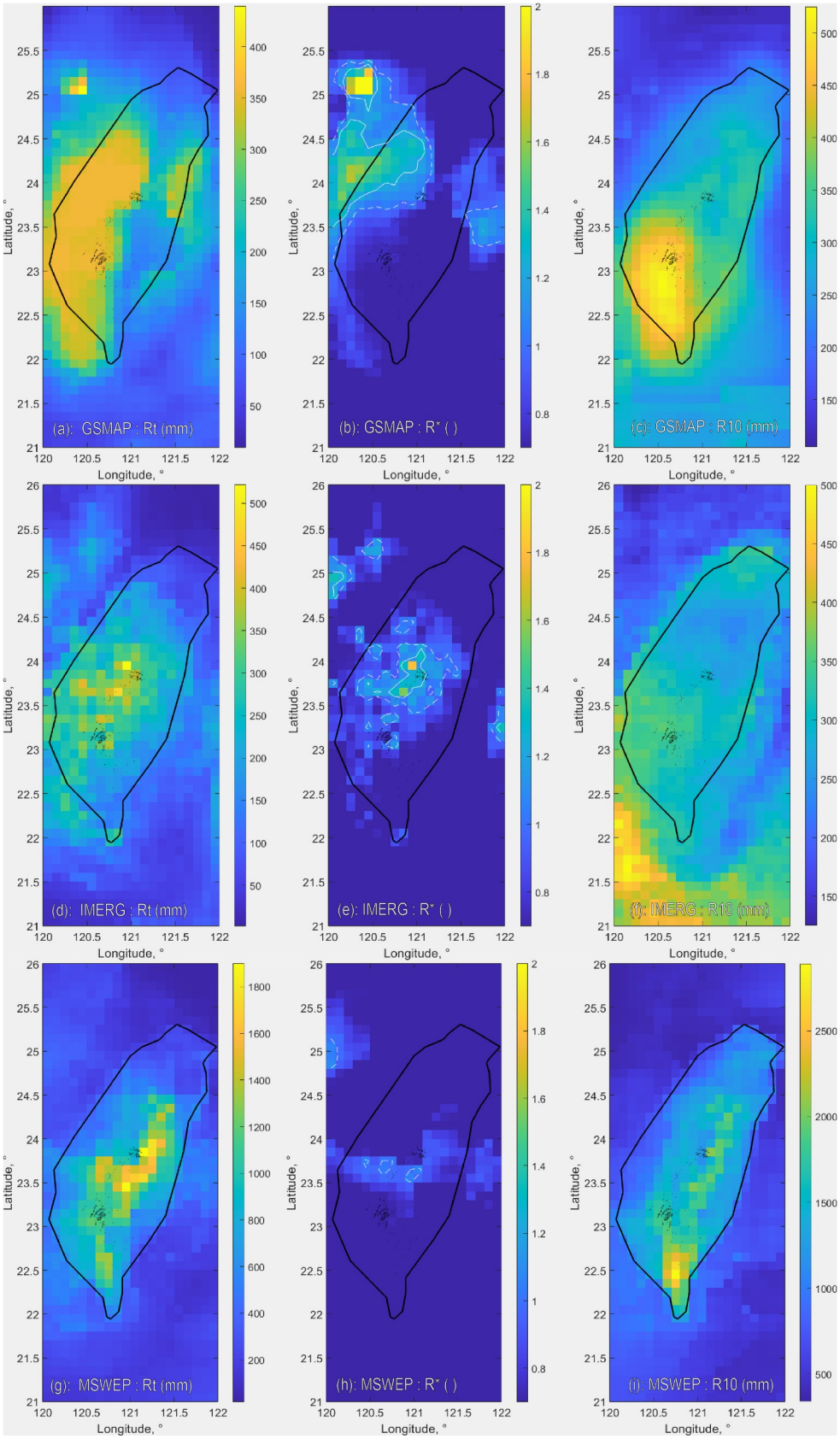

Figure S10 : Maps of the maximum total rainfall, Rt, (a,d,g), the rainfall anomaly, R*, (b,e,h) and the 10 year return rainfall, R10, (c,f,i) at the 12 h time scales for the TW8 event derived from GSMAP, IMERG and MSWEP, respectively. Note the different scales for Rt and R10.

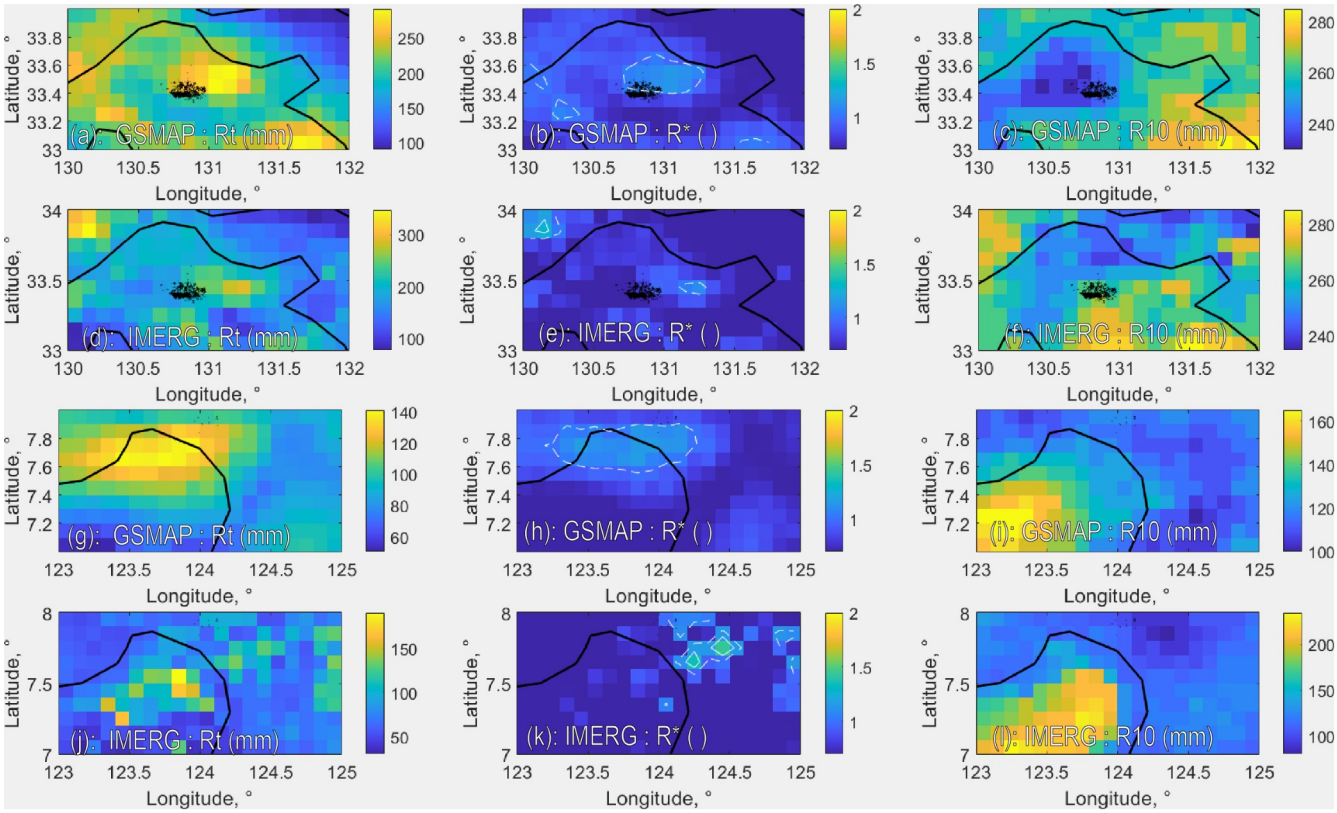

Figure S11 : Maps of the maximum total rainfall, Rt, (a,d), the rainfall anomaly, R*, (b,e) and the 10 year return rainfall, R10, (c,f) at the 48 h time scales for the J17 event derived from GSMAP and IMERG respectively. Maps of the maximum total rainfall, Rt, (g, j), the rainfall anomaly, R*, (h, k) and the 10 year return rainfall, R10, (i, l) at the 48 h time scales for the P17 event derived from GSMAP and IMERG respectively. Note the different scales for Rt and R10. MSWEP data was not available for P17 and did not detect any anomaly at any timescales for J17.

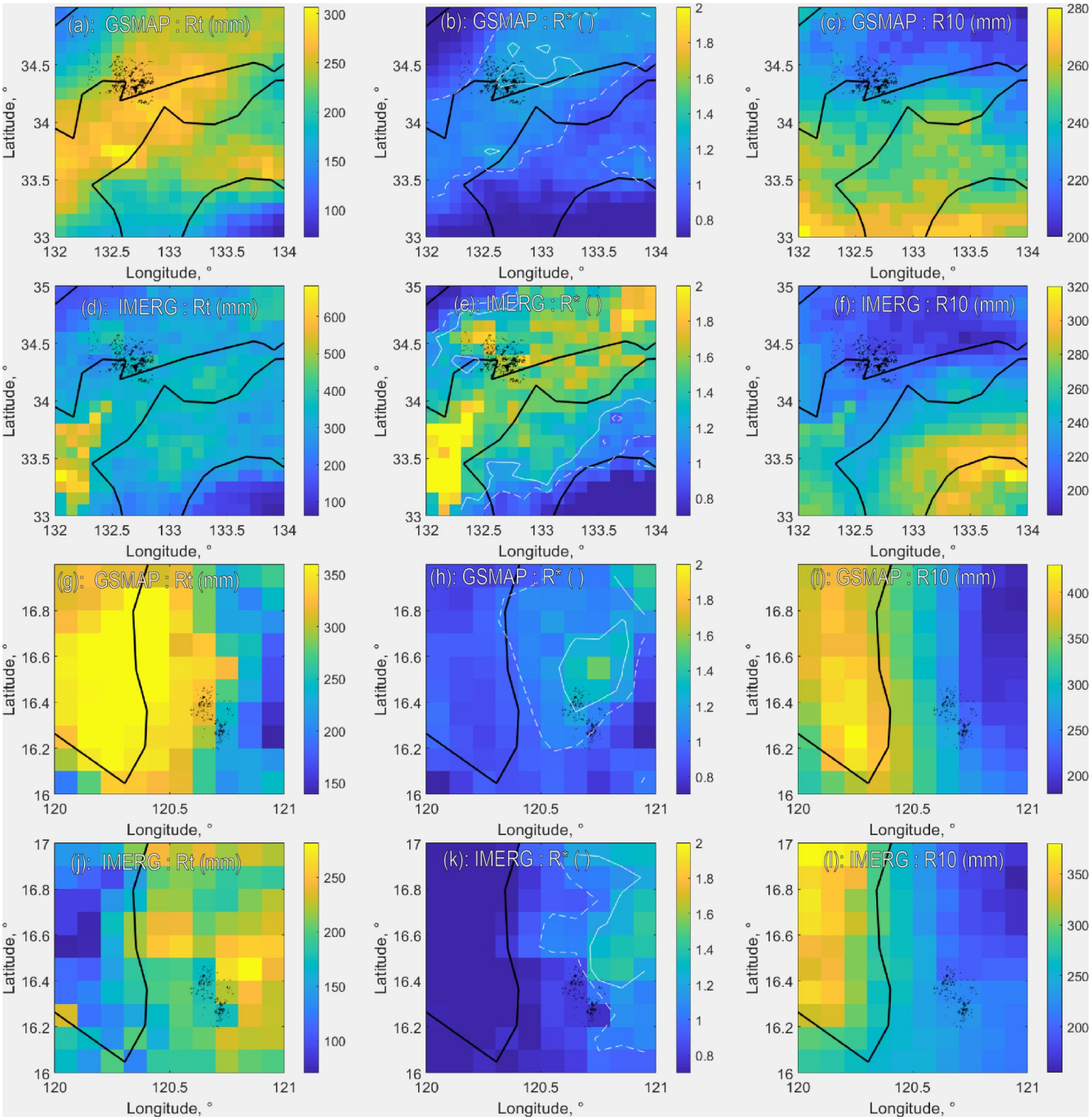

Figure S12 : Maps of the maximum total rainfall, Rt, (a,d), the rainfall anomaly, R*, (b,e) and the 10 year return rainfall, R10, (c,f) at the 48 h time scales for the J18 event derived from GSMAP and IMERG respectively. Maps of the maximum total rainfall, Rt, (g, j), the rainfall anomaly, R*, (h, k) and the 10 year return rainfall, R10, (i, l) at the 48 h time scales for the P18 event derived from GSMAP and IMERG respectively. Note the different scales for Rt and R10. MSWEP data was not available for these two cases.

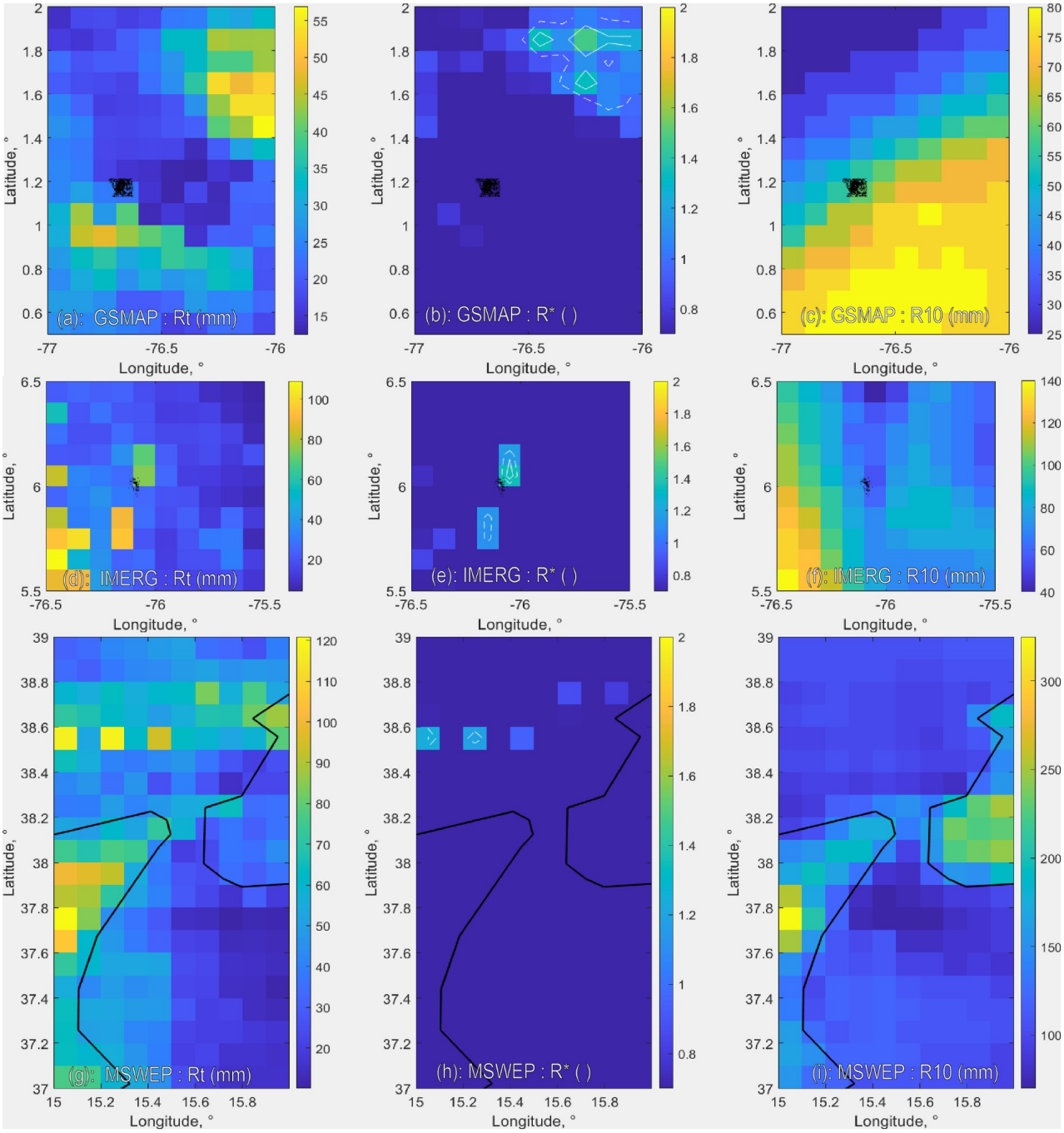

Figure S13 : Maps of the maximum total rainfall, Rt, (a,d,g), the rainfall anomaly, R*, (b,e,h) and the 10 year return rainfall, R10, (c,f,i) at the 3 h time scales for the C17 event derived from GSMAP, the C15 event derived from IMERG and the ITA event derived from MSWEP, respectively. Note the different scales for Rt and R10.

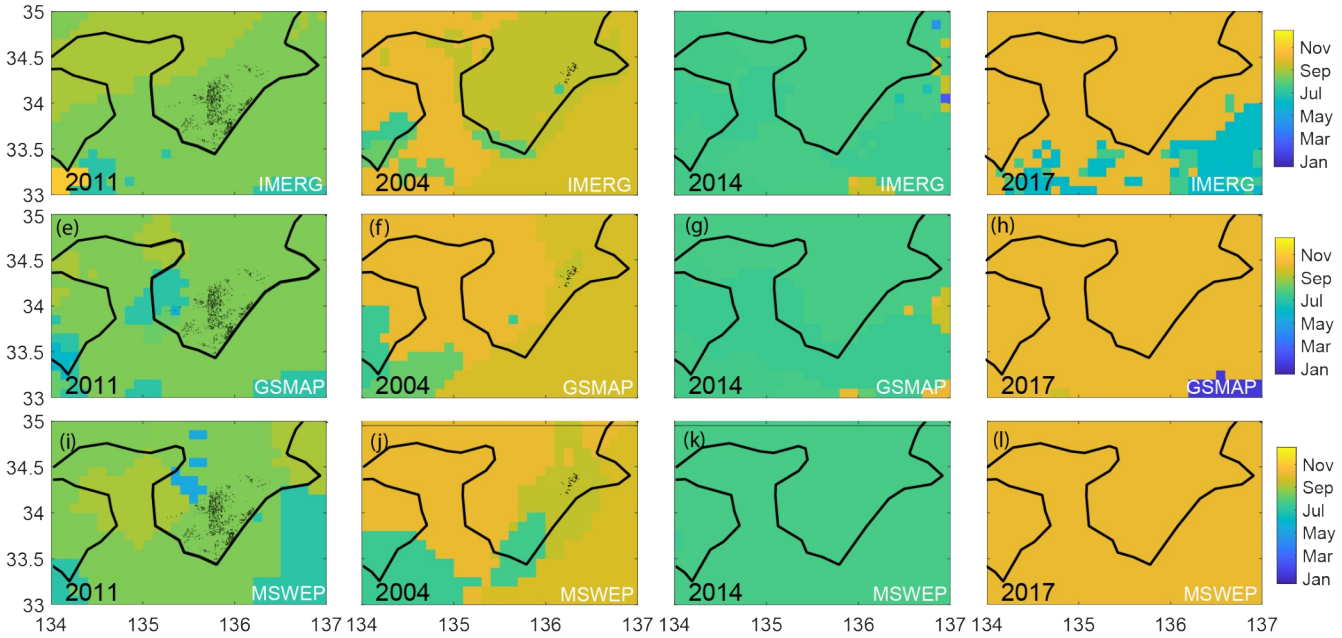

Figure S14: Timing of the 48h maximal rainfall anomalies for four years over the Kii Peninsula and for the three rainfall products. The anomalies are shown in Figure 2.

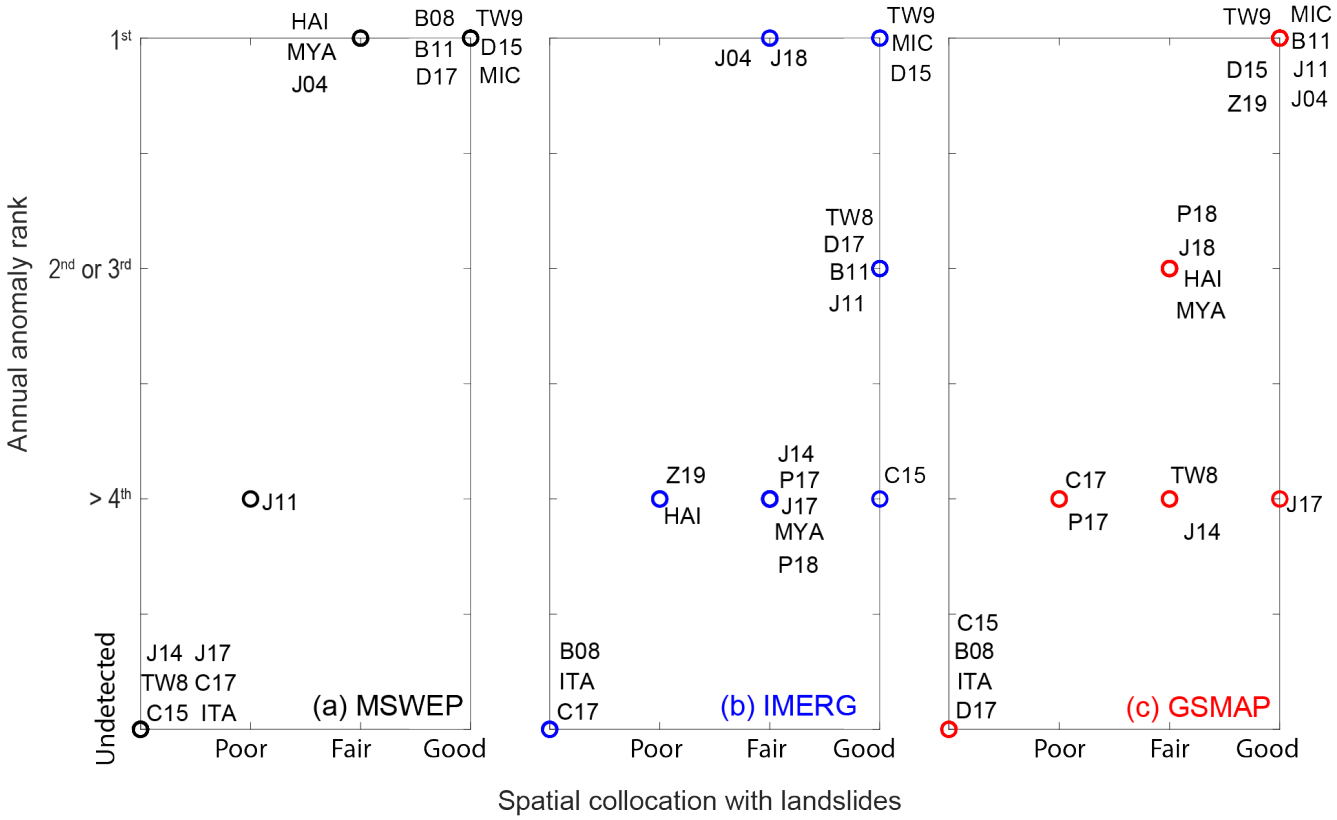

Figure S15 : Correlation between the spatial and temporal skills or rainfall anomalies of MSWEP (a), IMERG (b), and GSMAP (c). Note that MSWEP is only tested for 17 out of 20 case, excluding J18, P18 and Z19.

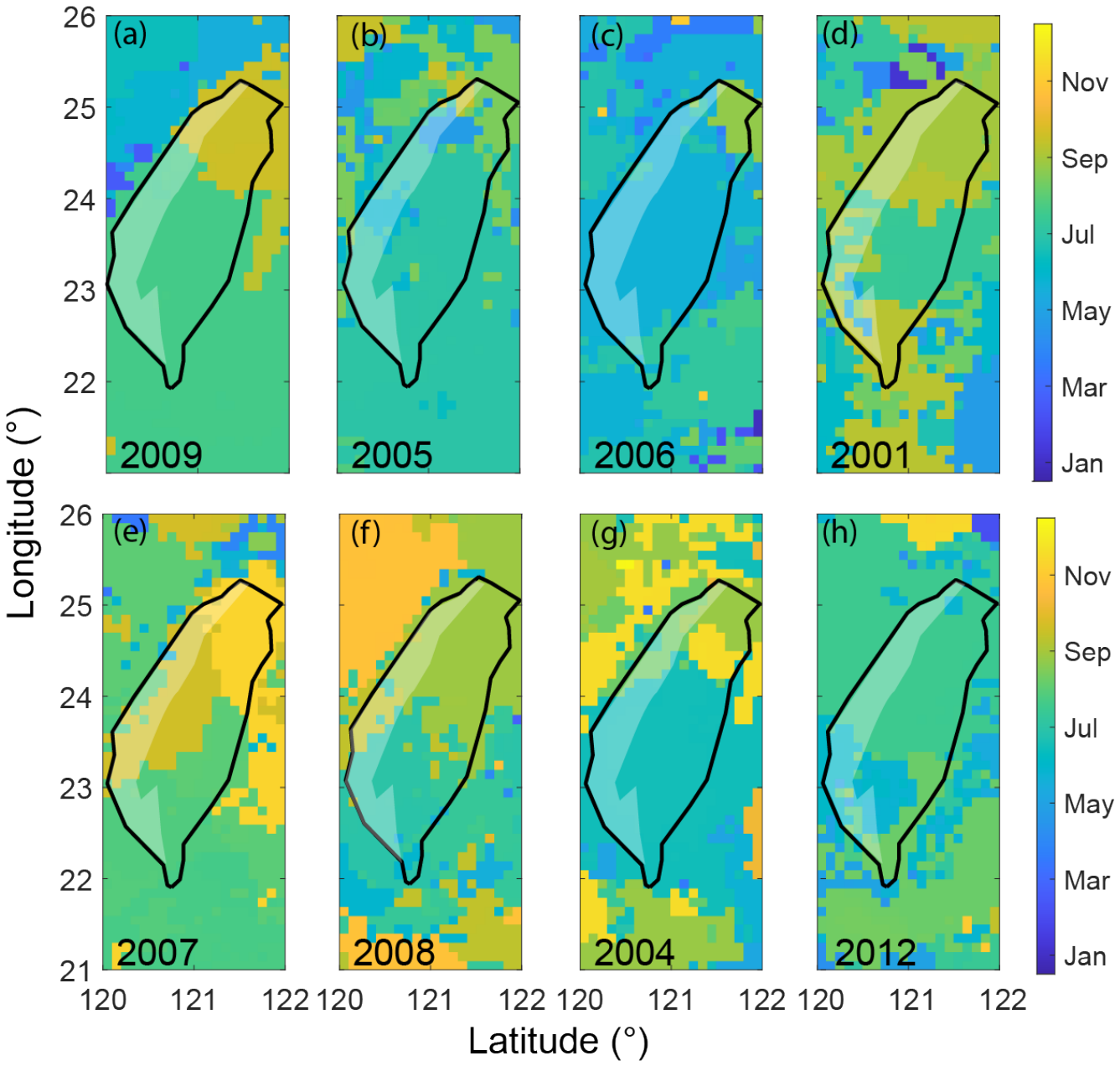

Figure S16: Timing of the 48h maximal rainfall anomalies from IMERG for eight years over Taiwan. The anomalies are shown in Figure 5.